

**Ge-Sb-Te based metasurface with angle-tunable switchable response in the telecom bands**A. I. Solomonov <sup>1,\*</sup> M. E. Bochkarev <sup>1,2</sup> S. I. Pavlov <sup>2</sup> P. I. Lazarenko <sup>3</sup> V. V. Kovalyuk <sup>4,5</sup> A. D. Golikov,<sup>4,5</sup>  
G. N. Goltsman,<sup>4,6</sup> S. A. Kozyukhin <sup>7</sup> S. A. Dyakov,<sup>8</sup> M. V. Rybin <sup>1,2</sup> and A. B. Pevtsov <sup>2,\*</sup><sup>1</sup>*School of Physics and Engineering, ITMO University, 197101, St. Petersburg, Russia*<sup>2</sup>*Ioffe Institute, 194021, St. Petersburg, Russia*<sup>3</sup>*National Research University of Electronic Technology, 124498, Zelenograd, Russia*<sup>4</sup>*National Research University Higher School of Economics, 101000, Russia*<sup>5</sup>*University of Science and Technology MISIS, 119049, Russia*<sup>6</sup>*Russian Quantum Center, 143025, Moscow, Russia*<sup>7</sup>*Institute of General and Inorganic Chemistry, 119991, Moscow, Russia*<sup>8</sup>*Skolkovo Institute of Science and Technology, 121205, Moscow, Russia*

(Received 15 December 2022; accepted 3 August 2023; published 21 August 2023)

Metasurfaces based on phase change materials are widely used for the controllable on-demand modification of properties of a device at the postfabrication stage. We report the fabrication of a switchable Ge-Sb-Te (GST)-based metasurface with a submicron period by magnetron sputtering with electron beam lithography postprocessing. We provide theoretical and experimentally measured angle-resolved reflection spectra of such metasurfaces. In these spectra, we observe magnetic dipole resonance features, which significantly differ for two different GST states, and Rayleigh anomalies, whose spectral position remains unchanged during the phase transition. We demonstrate the optical response of these metasurfaces to be strongly modulated under GST phase transition in the telecom wavelength range.

DOI: [10.1103/PhysRevB.108.085127](https://doi.org/10.1103/PhysRevB.108.085127)**I. INTRODUCTION**

Artificial electromagnetic structures known as metamaterials and their single-layer counterparts, metasurfaces, are highly attractive for various applications due to their unique optical response, which allows engineering invisible cloaks [1,2], complex light sources [3–6], wavefront controlling devices [7–10], and precise sensors [11–13]. Besides, metaoptics is associated with exotic effects such as the negative refractive index [14,15] and resonance-induced transparency [13,16,17] in various bands of the electromagnetic spectrum.

In modern metaphotonics, postfabrication tuning of the optical response is a significant challenge [18,19]. One of the possible dynamic switching methods is based on phase-change materials (PCM), which have two metastable states, amorphous and crystalline, coexisting under normal conditions [20–22]. Unlike most materials, PCM demonstrate nonvolatile phase transition. In the usual volatile case, the phase directly depends on the external conditions. However, PCM crystallization is a relatively slow process, which allows freezing the lattice disorder by rapid quenching. Thus, thermal heating is enough for the amorphous-to-crystal transition to occur. For this purpose, continuous-wave (CW)-laser radiation, Ohmic heating, or another treatment can be used. The reverse process requires an injection of energy high enough for lattice disorder to be induced, and the heat should be removed faster than the atoms find their sites in the crystal arrangement. This can be realized by optical means, using

high-energy femtosecond laser pulses [18]. Thus, heating the amorphous-phase material with short pulses was used to modify the disorder amount in a predictable manner, leading to the multilevel switching of a PCM [19]. Another remarkable peculiarity of PCMs is their unsaturated covalent bonds. Thus, the electrons are weakly confined by the host atoms and have a strong response to an applied electric field. As a result, PCMs have a relatively high permittivity [21]. Moreover, their permittivity can be doubled during phase transition, from 15 to 30. Nowadays, the most studied and used PCM is the germanium-antimony-tellurium alloy (Ge-Te-Sb or GST), which has found an application in rewritable data storage [20,22]. Moreover, this alloy is promising for device miniaturization [19] and on-demand control of spatial response properties [23–27]. Although GST has a relatively narrow band gap, which leads to absorption in the visible range, it is suitable for many applications in the infrared spectrum, including the range of 1.53–1.56  $\mu\text{m}$  (C-band), which is important for telecommunication fiber lines. Thus, switchable devices operating in the infrared range and empowered with metamaterials are very promising for a wide range of applications such as electrooptical modulators [28,29], conversion systems [30], and high-harmonic generation [25,31].

In this work, we demonstrate a PCM-based metasurface with a significant switching of optical response in the telecom band. The metasurface is an array of dielectric stripes made of the Ge-Sb-Te alloy. We simulate its angle-resolved reflection spectra and identify the features corresponding to the lattice-dependent Rayleigh anomaly, whose frequency does not change under the phase transition, and magnetic Mie-type resonances, which are strongly modified. The theoretical

\*aleksandr.solomonov@metalab.ifmo.ru

predictions are confirmed by experimental measurements of a GST metasurface sample.

## II. RESULTS AND DISCUSSION

### A. Fabrication of samples

Here, we consider a metasurface composed of GST stripes with a rectangular profile [Fig. 1(a)]. The samples were fabricated as follows. We produced amorphous  $\text{Ge}_2\text{Sb}_2\text{Te}_5$  thin films, using direct current (DC) magnetron sputtering with a commercially available polycrystalline target. The films were deposited onto a 0.1-mm-thick fused quartz substrate. The GST films thickness was 250 nm, according to atomic force microscopy (NT-MDT Solver Pro) measurements. Then, we fabricated GST stripes with electron beam lithography (Crestec CABL-9050C system) and reactive ion etching (Corial 200 setup). For the e-beam lithography, negative e-beam tone resist (ma-N2403) was employed. The reactive ion etching of GST film was performed in  $\text{SF}_6$  gas atmosphere and monitored *in situ* by a built-in reflectometer. We examined the etched samples with a broadband reflectometer (Filmetrics F-20 UVX) in lattice-free places. As a result, the structures with a period of  $P = 700$  nm and GST stripe widths of  $w = 500$  nm were fabricated. Scanning electron microscopy (SEM) images of the structure cross-section were obtained with a JEOL JSM 7001F microscope [Fig. 1(b)]. We studied the optical response of both amorphous and cubic crystalline GST structures. We obtained a crystallized GST structure by annealing the initial GST films at  $250^\circ\text{C}$  at a heating stage (HFS600E-PB4 Linkam) under argon flow. The annealing temperature was chosen based on the results of previous research [32].

### B. Experimental part

Next, we experimentally studied the fabricated metasurfaces by angle-resolved reflectance spectroscopy. The reflection measurements were performed over the spectral range of 900 to 2200 nm with an OceanOptics spectrometer equipped with an InGaAs-based charge-coupled detector. As a white light source, we used a tungsten-halogen lamp polarized by a Glan-Thompson prism. The metasurface samples were placed on a custom mount, which allowed us to vary the incidence angle in the range from 10 to 70 degrees. Figure 2 shows the reflection spectra normalized to that of a silver mirror.

For the crystalline-phase case, we observe asymmetric peaks, marked with blue and orange circles, which shift to longer wavelengths as the angle of incidence increases. Similar to the amorphous phase, the shape of these resonances changes for different angles of incidence. At the same time, in the range of 1850 to 1900 nm, we can observe a broadband resonance for different angles of incidence.

The experimental spectra in Fig. 3 confirm that our metasurface is capable of switching at the telecom wavelengths. Here, for the crystalline phase, a reflectance maximum is observed at  $\lambda = 1810$  nm, matching a local minimum in the amorphous phase spectrum. Moreover, an inverse effect is observed in the spectral region near the magnetic dipole of the amorphous phase (1400 to 1580 nm, which covers the telecom

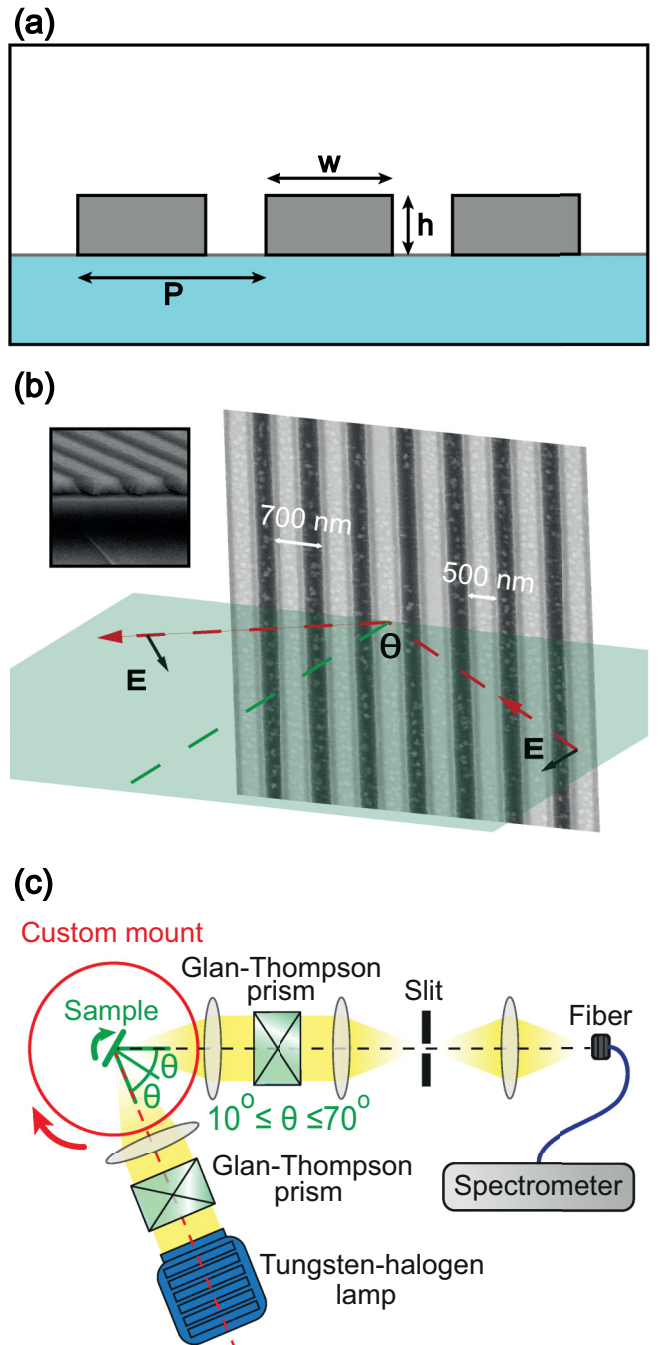


FIG. 1. (a) Schematic view of the GST metasurface. GST stripes (grey) are located on a silica substrate (cyan). (b) SEM image of the fabricated structure and the plane of incidence with the wave vectors of the incident and reflected waves. Inset shows a side view of the metasurface sample. (c) Experimental setup for reflection measurements.

S band); namely, an amorphous phase peak corresponds to low-intensity reflection for the crystalline phase.

### C. Theoretical analysis

To determine the origin of this features in reflection spectra, we theoretically studied the switchable metasurface using a rigorous coupled-wave analysis (RCWA) method [33–35].

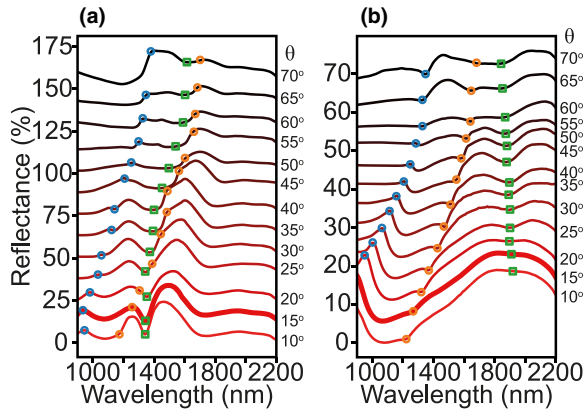


FIG. 2. Experimental reflection spectra of the metasurface for the (a) amorphous and (b) crystalline phases of GST. Blue and orange circles denote the air- and substrate-diffracting Rayleigh anomalies, respectively. Green squares indicate the magnetic dipole mode. All the curves are arbitrarily shifted in the vertical direction to facilitate comparison.

For our simulation, we measured the permittivity of GST (see Supplemental Material (SM) Fig. S1 [36]) in two phases after sample preparation by the spectral ellipsometry technique (HORIBA UVISSEL 2) using a five-layer model (air-surface-GST-SiO<sub>2</sub>-Si) and a single Tauc-Lorentz oscillator. We used the effective medium approximation for the rough surface layer [a mixture of the film (50%) and void (50%)]. We considered a linearly polarized wave incident from air at an angle  $\theta$  to the normal in the plane perpendicular to the strips [Fig. 1(b)]. The substrate made of fused silica ( $n = 1.5$ ) was also taken into account. The geometric dimensions of stripes were equal to those used in fabrication.

In high-index metasurfaces, guided modes are usually related to the Mie resonances supported by the constitutive elements. In our research, we considered a  $p$ -polarized wave [with the electric field vector in the plane of incidence, see

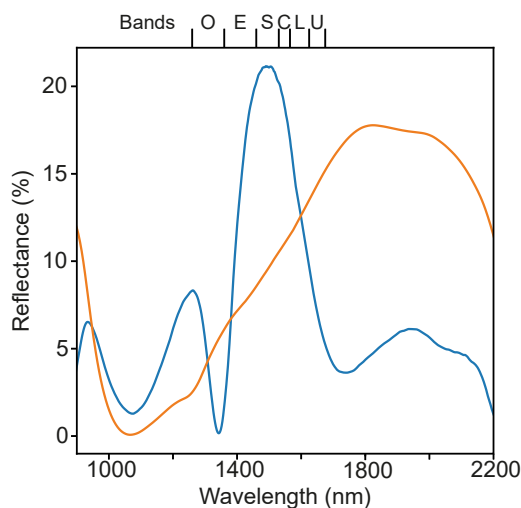


FIG. 3. Experimental reflection spectra for the amorphous (blue) and crystalline (orange) phases of GST for an incidence angle of  $\theta = 15^\circ$ . At the top, telecom bands are indicated.

the scheme in Fig. 1(b)] since it allows excitation of magnetic Mie resonances, which are located at lower frequencies than their electric counterparts [37]. Moreover, for  $s$ -polarization, the untunable Rayleigh anomaly affects the scattering much more strongly, interfering with the tunable Mie modes, which complicates the analysis.

In Figs. 4(a) and 4(b), we compare the simulated reflection spectra of the metasurface in two phases of GST. For both phases, two sets of asymmetric features are observed [blue and orange markers in Figs. 4, 5(c), and 5(d)], which are attributed to the opening of an additional diffraction channel [38]. These features are the so-called Rayleigh anomaly. The in-plane translational symmetry causes the longitudinal component to be preserved for any reciprocal lattice vector  $\mathbf{G}$ . The Laue equation reads  $\mathbf{k}_i = \mathbf{k}_s + \mathbf{G}$ , where  $\mathbf{k}_i$  and  $\mathbf{k}_s$  are the incident and scattered wave vectors, and  $G = 2\pi/P$  is the reciprocal lattice vector. Thus, the Rayleigh anomaly dispersion obeys the equation

$$n_d \sin \theta_d = n_i \sin \theta_i \pm m\lambda_r/P. \quad (1)$$

Here,  $\lambda_r$  is the wavelength of the Rayleigh feature,  $n_i$  and  $\theta_i$  are the refractive index of the first medium and the angle of incidence,  $n_d$  and  $\theta_d$  are the refractive index of the medium the light is diffracted to and the diffraction angle, and  $m$  is the diffraction order. Since the light is diffracted both forward (into the substrate) and backward (into air), a pair of Rayleigh anomalies are observed at the corresponding wavelengths. We should note that the anomalies are purely geometrical: they are defined only by the period of the structure and the incidence angle and have no dependence on the material parameters of the metasurface.

Of note, changing the term  $n_i$  in Eq. (1) leads to a shift of Rayleigh anomalies, even when the geometrical parameters are kept. This effect is known as index-matching and observed in metallic gratings [39]. Moreover, when the indexes of the substrate and superstrate are equal, the resonances become sharper (see SM Fig. S3 [36]), and therefore, for a practical application, both the substrate and superstrate of a device should be made of the same material.

For the amorphous phase, when the magnetic field is located inside the stripes, the simulations show a narrow dip, associated with the magnetic dipole mode [see the green square markers in Figs. 4, 5(c), and 5(d)]. The electromagnetic field profiles are shown in Figs. 5(a) and 5(b). In particular, for  $\theta = 10^\circ$ , the dip is located at 1533 nm. As the incidence angle increases, the dip red-shifts. For the crystalline phase, there is only one peak in the spectrum in the range of 2000 to 2250 nm, which corresponds to the low-wavelength side of the magnetic dipole, manifesting itself as a Fano resonance.

In Fig. 4(c), we analyze how different values of the GST crystallization fraction affect the spectrum. Here we employ the Lorentz-Lorenz relation used for evaluating the GST permittivity during multilevel switching, i.e., for different amounts of the lattice disorder [40]

$$\frac{\varepsilon_{\text{eff}} - 1}{\varepsilon_{\text{eff}} + 2} = \delta \frac{\varepsilon_c - 1}{\varepsilon_c + 2} + (1 - \delta) \frac{\varepsilon_a - 1}{\varepsilon_a + 2}, \quad (2)$$

where  $\delta$  is the fraction of the crystalline-phase GST, ranging from 0 to 1, and  $\varepsilon_a$  and  $\varepsilon_c$  are the permittivities of the amorphous and crystalline phases, respectively. For this notation,

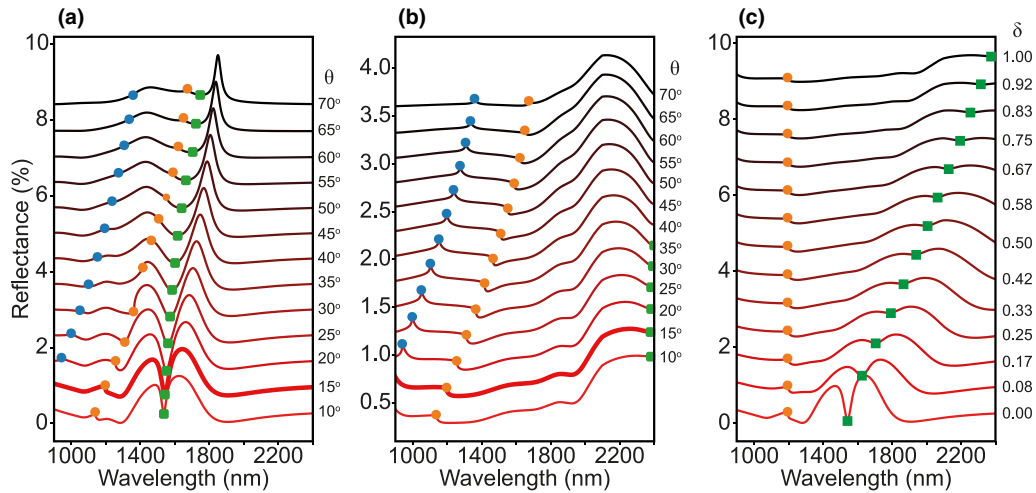


FIG. 4. Simulated reflection spectra of metasurface for the (a) amorphous and (b) crystalline phases of GST. (c) Evolution of the reflection spectrum for an incidence angle of  $15^\circ$  for metasurfaces with different crystallization fractions of GST. Blue and orange circles denote Rayleigh anomalies corresponding to the waves diffracted into air and the substrate, respectively. Green squares indicate the magnetic dipole mode. All the spectra are shifted in the vertical direction to facilitate comparison.

$\delta = 0$  corresponds to the amorphous phase with the highest amount of lattice disorder right after the sample fabrication, and  $\delta = 1$ , to the crystalline phase.

The reflection spectra for these two measured values for the amorphous and crystalline phase are shown in Figs. 4(a) and 4(b), respectively. Figure 4(c) shows the dependence of

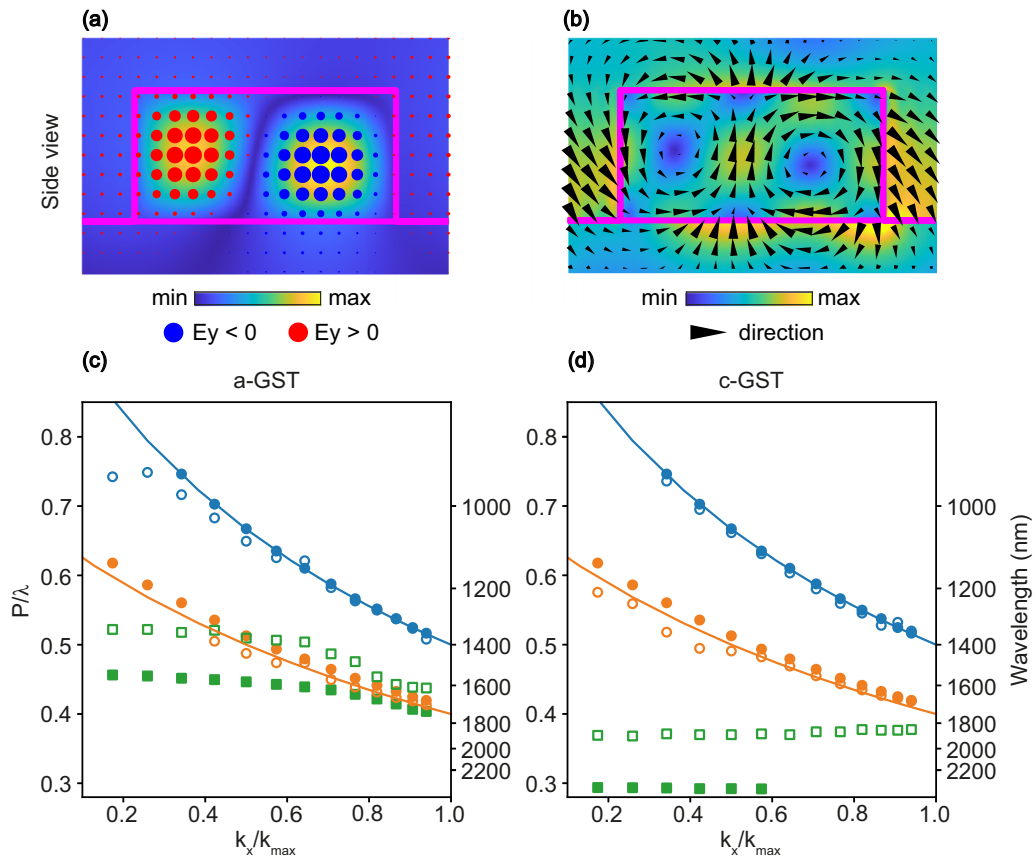


FIG. 5. Distribution of the (a) electric and (b) magnetic fields of the magnetic dipole mode for an incidence angle of  $10^\circ$ . Theoretical and experimental dispersion of the Rayleigh anomaly and magnetic dipole mode for the (c) amorphous and (d) crystalline phases of GST. Blue and orange circles indicate the Rayleigh anomalies corresponding to the waves diffracted into air and the substrate, respectively. Green squares indicate the magnetic dipole mode. Open and closed markers indicate the experimental and theoretical data, respectively. Lines are the exact solution for the Rayleigh anomalies.

the reflection spectra on the crystallization fraction of GST for  $\theta = 15^\circ$ . It is clearly seen that the Rayleigh anomaly at 1194 nm is independent of the crystallization fraction  $\delta$  since its spectral position is defined by the equation containing the metasurface period only. The magnetic dipole feature red-shifts as the fraction  $\delta$  increases, which is explained by changing real part of the permittivity. In particular, according to the ellipsometry results, the real part of the permittivity changes from 17 for amorphous to 47 for crystalline phase at  $\lambda = 1540$  nm. Moreover, the imaginary part of the permittivity also increases from  $\text{Im}(\epsilon_a) \approx 0.3$  to  $\text{Im}(\epsilon_c) \approx 17$  after the phase transition, causing the Q-factor of the mode to decay. Although Eq. (2) is derived with simple approximations, it is used for the description of multilevel switching of GST. Our purpose here is just to identify peaks through their evolution. This task does not require the accurate value of the GST permittivity for the intermediate phase.

### III. CONCLUSION

We fabricated metasurfaces made of both amorphous and crystalline  $\text{Ge}_2\text{Sb}_2\text{Te}_5$  in the form of gratings with a submicron period, using magnetron sputtering and e-beam lithography postprocessing. We studied angle-resolved reflection spectra of the synthesized metasurfaces in the infrared range theoretically and experimentally, and these results are

in good agreement. We revealed that the observed spectral features are associated with Rayleigh anomalies and magnetic dipole resonance. We demonstrated that the optical response of the metasurface is significantly modulated under the phase transition of  $\text{Ge}_2\text{Sb}_2\text{Te}_5$ . In the range of 1400 to 1600 nm, which covers the telecom bands, the intensity of the optical response of the amorphous phase was double that of its crystalline counterpart, and in the range of 1600 to 2200 nm, we observed an opposite effect, namely, the crystalline-phase optical response was three times higher than the amorphous one. For GST with a thickness of several hundred nanometers, phase switching can be realized by means of short optical or electric pulses at the postfabrication stage, which is crucial for practical applications. Thus, such a PCM-based metasurface is potentially promising for switchable devices providing control over light flows.

### ACKNOWLEDGMENTS

The samples were fabricated with contributions from the research laboratory “Materials and devices for active photonics” (FSMR-2022-0001). The theoretical part of this work was supported by the Russian Science Foundation (Project No. 21-79-10214). The experimental investigations of the work were carried out with financial support within the framework of the institute Agreement No. 0040-2019-0012.

- 
- [1] W. Cai, U. K. Chettiar, A. V. Kildishev, and V. M. Shalaev, *Nat. Photonics* **1**, 224 (2007).
- [2] F. Martinez and M. Maldovan, *Mater. Today Phys.* **27**, 100819 (2022).
- [3] S. Liu, A. Vaskin, S. Addamane, B. Leung, M.-C. Tsai, Y. Yang, P. P. Vabishchevich, G. A. Keeler, G. Wang, X. He, Y. Kim, N. F. Hartmann, H. Htoon, S. K. Doorn, M. Zilk, T. Pertsch, G. Balakrishnan, M. B. Sinclair, I. Staude, and I. Brener, *Nano Lett.* **18**, 6906 (2018).
- [4] A. Vaskin, R. Kolkowski, A. F. Koenderink, and I. Staude, *Nanophotonics* **8**, 1151 (2019).
- [5] S. I. Pavlov, S. A. Dyakov, A. I. Solomonov, A. V. Nashchekin, N. A. Feoktistov, N. A. Gippius, S. G. Tikhodeev, A. K. Samusev, and A. B. Pevtsov, *Photonics Nanostruct. Fundam. Appl.* **48**, 100975 (2022).
- [6] O. M. Kushchenko, D. S. Gets, M. V. Rybin, D. A. Yavsin, S. V. Makarov, I. I. Shishkin, and A. D. Sinelnik, *Laser Photonics Rev.* **2200836** (2023).
- [7] N. I. Landy, S. Sajuyigbe, J. J. Mock, D. R. Smith, and W. J. Padilla, *Phys. Rev. Lett.* **100**, 207402 (2008).
- [8] M. V. Rybin, A. V. Zherzdev, N. A. Feoktistov, and A. B. Pevtsov, *Phys. Rev. B* **95**, 165118 (2017).
- [9] D. O. Ignatyeva, D. Karki, A. A. Voronov, M. A. Kozhaev, D. M. Krichevsky, A. I. Chernov, M. Levy, and V. I. Belotelov, *Nat. Commun.* **11**, 5487 (2020).
- [10] O. Yermakov, H. Schneidewind, U. Hübner, T. Wieduwilt, M. Zeisberger, A. Bogdanov, Y. Kivshar, and M. A. Schmidt, *ACS Photonics* **7**, 2834 (2020).
- [11] S. Yoo and Q.-H. Park, *Nanophotonics* **8**, 249 (2019).
- [12] A. S. Saadeldin, M. F. O. Hameed, E. M. A. Elkaramany, and S. S. A. Obayya, *IEEE Sens. J.* **19**, 7993 (2019).
- [13] J. Zhong, X. Xu, and Y.-S. Lin, *Nanomaterials* **11**, 2175 (2021).
- [14] F. Ling, Z. Zhong, R. Huang, and B. Zhang, *Sci. Rep.* **8**, 1 (2018).
- [15] T. Suzuki, M. Sekiya, T. Sato, and Y. Takebayashi, *Opt. Express* **26**, 8314 (2018).
- [16] M. F. Limonov, M. V. Rybin, A. N. Poddubny, and Y. S. Kivshar, *Nat. Photonics* **11**, 543 (2017).
- [17] Z. Song, Z. Song, Z. Song, A. Chen, A. Chen, J. Zhang, J. Wang, and J. Wang, *Opt. Express* **27**, 25196 (2019).
- [18] S. V. Makarov, A. S. Zalogina, M. Tajik, D. A. Zuev, M. V. Rybin, A. A. Kuchmizhak, S. Juodkakis, and Y. Kivshar, *Laser Photonics Rev.* **11**, 1700108 (2017).
- [19] P. Tonkaev, I. S. Sinev, M. V. Rybin, S. V. Makarov, and Y. Kivshar, *Chem. Rev.* **122**, 15414 (2022).
- [20] M. Wuttig and N. Yamada, *Nat. Mater.* **6**, 824 (2007).
- [21] S. Raoux, *Annu. Rev. Mater. Res.* **39**, 25 (2009).
- [22] S. Kozyukhin, P. Lazarenko, A. Popov, and I. Eremenko, *Russ. Chem. Rev.* **91**, 1 (2022).
- [23] N. I. Zheludev and Y. S. Kivshar, *Nat. Mater.* **11**, 917 (2012).
- [24] B. Gholipour, A. Karvounis, J. Yin, C. Soci, K. F. MacDonald, and N. I. Zheludev, *NPG Asia Materials* **10**, 533 (2018).
- [25] M. V. Rybin, A. D. Sinelnik, M. Tajik, V. A. Milichko, E. V. Ubyivovk, S. A. Yakovlev, A. B. Pevtsov, D. A. Yavsin, D. A. Zuev, and S. V. Makarov, *Laser Photonics Rev.* **16**, 2100253 (2022).
- [26] A. Barreda, C. Zou, A. Sinelnik, E. Menshikov, I. Sinev, T. Pertsch, and I. Staude, *Opt. Mater. Express* **12**, 3132 (2022).
- [27] P. Lazarenko, V. Kovalyuk, P. An, S. Kozyukhin, V. Takáts, A. Golikov, V. Glukhenkaya, Y. Vorobyov, T. Kulevov, A. Prokhodtsov, A. Sherchenkov, and G. Goltsman, *Acta Mater.* **234**, 117994 (2022).

- [28] Z. Yu, J. Zheng, P. Xu, W. Zhang, and Y. Wu, *IEEE Photonics Technol. Lett.* **30**, 250 (2017).
- [29] M. Singh, S. K. Raghuvanshi, and T. Srinivas, *Phys. Lett. A* **383**, 3196 (2019).
- [30] I. Alamgir, F. St-Hilaire, and M. Rochette, *Opt. Lett.* **45**, 857 (2020).
- [31] M. Zhu, S. Abdollahramezani, T. Fan, and A. Adibi, *Opt. Lett.* **46**, 5296 (2021).
- [32] P. Lazarenko, V. Kovalyuk, P. An, A. Prokhotsov, A. Golikov, A. Sherchenkov, S. Kozyukhin, I. Fradkin, G. Chulkova, and G. Goltsman, *APL Mater.* **9**, 121104 (2021).
- [33] S. G. Tikhodeev, A. L. Yablonskii, E. A. Muljarov, N. A. Gippius, and T. Ishihara, *Phys. Rev. B* **66**, 045102 (2002).
- [34] M. G. Moharam, E. B. Grann, D. A. Pommet, and T. K. Gaylord, *J. Opt. Soc. Am. A* **12**, 1068 (1995).
- [35] S. Han, L. Cong, Y. K. Srivastava, B. Qiang, M. V. Rybin, A. Kumar, R. Jain, W. X. Lim, V. G. Achanta, S. S. Prabhu, Q. J. Wang, Y. S. Kivshar, and R. Singh, *Adv. Mater.* **31**, 1901921 (2019).
- [36] See Supplemental Material at <http://link.aps.org/supplemental/10.1103/PhysRevB.108.085127> for measured dielectric permittivities of GST; demonstration of the Rayleigh anomaly which becomes stronger if it is tuned with Mie resonance; a demonstration of the pair Rayleigh anomaly which are tunes when the index-matching condition is met.
- [37] T. Liu, R. Xu, P. Yu, Z. Wang, and J. Takahara, *Nanophotonics* **9**, 1115 (2020).
- [38] S. A. Dyakov, N. A. Gippius, M. M. Voronov, S. A. Yakovlev, A. B. Pevtsov, I. A. Akimov, and S. G. Tikhodeev, *Phys. Rev. B* **96**, 045426 (2017).
- [39] C. Zhang, C. Zhang, C. Zhang, Z. Wu, Z. Wu, Q. Wang, and Q. Wang, *Opt. Mater. Express* **12**, 2824 (2022).
- [40] C. H. Chu, M. L. Tseng, J. Chen, P. C. Wu, Y.-H. Chen, H.-C. Wang, T.-Y. Chen, W. T. Hsieh, H. J. Wu, G. Sun, and D. P. Tsai, *Laser Photonics Rev.* **10**, 986 (2016).